8-2022

Experimental Evaluation of a 63.3:1 Dual-Stage Coaxial Magnetic Gear

Hossein Baninajar
Portland State University, hossein@pdx.edu

Sina Modaresahmadi
University of North Carolina at Charlotte

H. Y. Wong

Jonathan Bird
Portland State University, bird@pdx.edu

W. Williams

See next page for additional authors

Citation Details

Published as: Baninajar, H., Modaresahmadi, S., Wong, H. Y., Bird, J. Z., Williams, W., & Dechant, B. (2022). Experimental Evaluation of a 63.3: 1 Dual-Stage Coaxial Magnetic Gear.

Authors

Hossein Baninajar, Sina Modaresahmadi, H. Y. Wong, Jonathan Bird, W. Williams, and B. Dechant

This article has been accepted for publication in IEEE Transactions on Energy Conversion. This is the author's version which has not been fully edited and content may change prior to final publication. Citation information: DOI 10.1109/TEC.2022.3190831

Experimental Evaluation of a 63.3:1 Dual-Stage Coaxial Magnetic Gear

H. Baninajar, S. Modaresahmadi, H. Y. Wong, J. Z. Bird, W. Williams, B. Dechant

Abstract- **This paper presents the construction and testing results for a 63.3:1 dual-stage coaxial magnetic gear for use in a marine hydrokinetic generator demonstrator application. The dual-stage magnetic gear is composed of series-connected coaxial magnetic gear. The stage-2 magnetic gear utilizes Halbach magnet arrays on both rotors and has a 9.5:1 gear ratio. The stage-1 magnetic gear utilizes a Halbach rotor on the outer rotor and a flux concentration inner rotor. The stage-1 magnetic gear has a 6.67:1 gear ratio and at the peak torque of 1220Nm the stage-1 MG was shown to be capable of operating with a 268 N·m/L torque density at 45 r/min and with 95% peak efficiency. The dual-stage magnetic gear was shown to be able to operate with a peak torque density of 228.6 N·m/L and with an 87% efficiency at 45 r/min input speed. The measured efficiency was significantly lower than what was calculated, and the increased losses are believed to be primarily due to the electrical losses induced within the magnetic gears conductive support components.**

***Index Terms*-- Finite-element analysis, Halbach rotor, magnetic gear, wave energy converter.**

I. INTRODUCTION

THE design of a rotary-based generator for a wave energy converter (WEC) application is extremely challenging because the rotary speeds created by the ocean are very low, typically less than 45 r/min, and the torque is extremely high. As mechanical gearboxes have high torque densities, they are often considered for use in WEC generators [1, 2]. However, gearboxes can suffer from long-term reliability issues. For example, gearbox failures have been one of the leading causes for wind turbine drivetrain downtime [3]. Therefore, the reliance on mechanical gears within even more remotely located WEC environments creates significant reliability concerns.

The main alternative to the mechanical gearbox is the direct-drive permanent magnet (PM) generator. The use of a PM generator removes the potential for gearbox teeth failure and lubrication requirements. However, as the shear stress and torque density of a PM generator is thermally limited by current, a PM generator does not normally operate at a magnetic shear stress above 20-40 kN/m^2 [4]. This results in the PM-generator not achieving a continuous operating torque density above ~ 50 N·m/L [5, 6]. Using a dual air-gap can increase a PM-generators' torque density. For instance, Li *et. al.* showed that a dual-airgap Vernier motor can achieve a 66 N·m/L torque density with a 0.84 power factor [7, 8]. However, this is still well below the torque density of a mechanical gear. To try to make the WEC generator more reliable, and also reduce the levelized cost of energy [9, 10], several authors have recently proposed using magnetic gearing [11-18].

Coaxial magnetic gears (MGs) use a contactless mechanism for speed amplification [19, 20], they do not need gear lubrication and have inherent overload protection. As a coaxial MG contains two sets of rotors with magnets the airgap shear stress can be very high [21], MGs with torque densities above 200 Nm/L have been demonstrated [22],[23]. Unlike with a mechanical gear if excessive torque is applied to a MG the rotor poles slip rather than catastrophically failing. The losses within a MG are also frequency dependent and therefore for low-speed, high-torque, applications a MG offers the potential for increased efficiency and reduced electrical material cost [24].

A number of authors have recently tested MG generators for WEC applications, for instance, Johnson *et al.* presented a radially configured MG generator prototype that achieved an 82.8 N·m/L torque density and had a 11.33:1 gear ratio [16]. Whilst Kouhshahi *et al.* presented a flux-focusing axial MG with a 4.16:1 gear ratio and reported 94.4 N·m/L torque density [18]. As the oceans frequency is very low, most marine hydrokinetic generators such as tidal generators [25], heaving WEC generators [26] and oscillating surge WECs [27] will benefit from using a much higher gear ratio.

An increase in gearing ratio can be achieved by integrating a Vernier motor with a MG. For example Zhang *et al.* [28] tested a 34:1 magnetically gearing motor that combined a 4.25:1 gear ratio MG with a 8:1 gear ratio Vernier motor. However, relying on a Vernier motor for gearing limits the torque capability, since the airgap field is created by only one set of rotor magnets. Zhang *et al.* integrated MG Vernier motor had a peak torque density of only 18 N·m/L [28]. This is comparable to many off-the-shelf PM-motors [6].

To achieve higher coaxial MG gear ratios with a high torque density the use of dual-stage nested [29-33] and series connected coaxial MGs [15, 32-38] have been proposed. The use of a nested MG appears compact because the high-speed inner MG stage can be coupled radially with a higher torque lower speed outer rotor stage. However, if the mechanical construction of the MG is studied [32] one can note that the mechanical

---

This work was funded in part by the Office of Energy Efficiency and Renewable Energy (EERE), U.S. Department of Energy, under Award Number DE-EE0008100.

H. Baninajar, H. Y. Wong, J. Bird and B. Dechant are with the Department of Electrical Computer Engineering, Portland State University, Portland, OR, 97201 USA (e-mail: hossein@pdx.edu, h28@pdx.edu, jonathan.bird@ieee.org bdechant@pdx.edu).

S. Modaresahmadi and W. Williams are with the Department of Engineering Technology, University of North Carolina at Charlotte, Charlotte, NC, USA 28269. (email: smodares@alumni.uncc.edu, wbwillia@uncc.edu)

This article has been accepted for publication in IEEE Transactions on Energy Conversion. This is the author's version which has not been fully edited and content may change prior to final publication. Citation information: DOI 10.1109/TEC.2022.3190831

support structure needs to nest three rotors, all rotating relative to each other, as well as two stationary rotors. The need to provide the embedded bearing supports for each rotor as well as nested rotor end-plate housing supports leads to a relatively long axial length. The nested design is also challenging to magnetically design because the inner MG stage's radial field must be prevented from entering the outer MG stage.

A multistage series connected MG is simpler to design as each stage can be designed independent of each other and it provides greater interoperability. Li *et al.* was the first to test a dual-stage series connected coaxial MG, Li tested a 59:1 dual-stage MG that consisted of a 6.45:1 and 9.14:1 MGs connected in series [32, 39]. The dual-stage MG was shown to achieve a combined 118 N·m/L torque density [39]. However, the experimental testing also showed that the design had very high losses. The losses were caused by the non-torque producing higher spatial harmonics created by the flux-focusing rotor fields. And large eddy current losses were created in the axial end-plate rotor supports [35, 39]. The MG radial fields that are not passing through the modulator slots tend to splay out axially and when the end plates are conductive this leads to increased edge-effect eddy-current losses. This is not typically observed in PM-motors.

This paper reports on the design, building and testing of a new type of 63.3:1 dual-stage coaxial MG for a WEC proof-of-principle demonstrator. A cut-away view of the dual-stage design is shown in Fig. 1 and the magnet and modulator geometry used in both MG stages is shown in Fig. 2. To improve the MG performance both MGs utilize an outer rotor Halbach magnet array. The stage-1 inner MG rotor used a flux concentrating rotor typology [40, 41] and the stage-2 MG inner rotor used a 4-segment Halbach rotor arrangement. The flux concentration rotor arrangement was used in the stage-1 inner rotor because the inner rotor magnets were large in size. The flux-concentration rotor also helped with the magnet assembly since the magnets can be inserted into the ferromagnetic slots. A torque performance comparison of the flux concentration MG is discussed in [41, 42].

The stage-1 MG contained $p_{Ii} = 6$ inner rotor pole-pairs, $p_{Io} = 40$ outer rotor pole-pairs and the number of central cage rotor modulator slots, n_I, was selected to satisfy:

$$n_I = p_{Ii} + p_{Io} \tag{1}$$

With (1) met the angular speed relationship between each rotor is [19, 20]

$$p_{Ii}\omega_{Ii} = n_I\omega_I - p_{Io}\omega_{Io} \tag{2}$$

The central modulator torque, T_I is the highest since it is related to the outer rotor torque, T_{Io}, by $T_I = T_{Io} \cdot n_I / p_{Io}$. However, in this design the central rotor was fixed, $\omega_I = 0$, as this can allow the MG to be hermetically sealed [14]. In this case

$$\omega_{Ii} = -G_I\omega_{Io} \tag{3}$$

where the gear ratio is $G_I = p_{Io}/p_{Ii}$. With $(p_{Ii}, n_I, p_{Io}) = (6, 46, 40)$ the stage-1 gear ratio is $G_I = 40/6 = 6.67$. It can be noted that this (6, 46, 40) pole combination is divisible by two, thereby providing 180° symmetry. The pole values are based off a (3, 23, 20) combination and as both 3 and 23 are prime numbers this results in a low torque ripple.

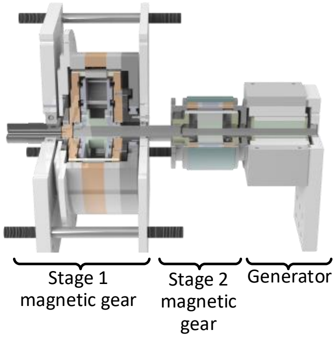

Fig. 1. Cut-through view showing the dual-stage magnetically gear generator with the stage 1, stage 2 and generator connected in series.

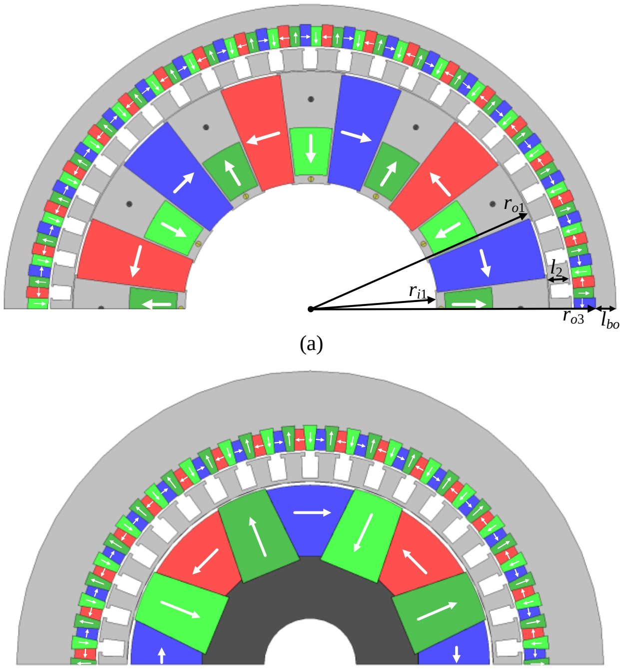

(a)

(b)

Fig. 2. (a) A half cut-through view of the stage-1 MG geometric design [14] and (b) the stage-2 MG design [15].

The stage-2 MG contained $p_{IIi} = 4$ inner rotor pole-pairs, $n_{II} = 38$ modulator slots, and $p_{IIo} = 34$ outer pole-pairs. Satisfying

$$n_{II} = p_{IIi} + p_{IIo} \tag{4}$$

and holding the outer rotor fixed, $\omega_{IIo} = 0$, the relationship between the inner rotor angular speed, ω_{IIi}, and central-cage rotor angular speed, n_{II}, is

$$\omega_{IIi} = G_{II}\omega_{II} \tag{5}$$

where $G_{II} = n_{II}/p_{IIi} = 9.5$. Combining gear ratios, the dual-stage MG creates the angular speed change described by

$$\omega_{IIi} = G_r\omega_{Io} \tag{6}$$

where $G_r = G_I G_{II} = 63.\dot{3}$. Table I shows the selected design requirement for the proof-of-principle dual-stage MG. A detailed discussion on the parameter design for the stage-1 and stage-2 MG is provided in [14] and [15] respectively.

TABLE I. TARGET SPECIFICATIONS FOR THE STAGE-1 AND STAGE-2 MG.

Requirement		Value	Unit
Stage 1	Input speed, ω_{Io}	≤ 45	r/min
	Rated power	5	kW
	Input torque, T_{Io}	≥1061	N·m
	Gear ratio, G_I	$6.6\dot{6}$	-
Stage 2	Output speed, ω_{IIi}	2850	r/min
	Efficiency	≥93	%
	Torque ripple	≤3	%
	Input rotor torque, T_{IIc}	≥159.2	N·m
	Output rotor torque, T_{IIi}	≥16.7	N·m
Gear ratio, G_r		63.3	-

II. MAGNETIC GEAR DESIGNS

The geometric values used for both the stage-1 MG and stage-2 MG are shown in Table II. The MG designs used M-19 electrical steel laminations and N-48 magnet grade in both MG stages. The stage-1 MG has a larger outer rotor airgap length, g_o = 1.5 mm, because the initial intention was to provide space to apply a sealing coating to create a hermetic seal around the outside of the modulator thereby preventing the possibility of water ingress into the stage-1 inner rotor as well as the stage-2 MG and generator. This design arrangement is shown in [14]. Due to mechanical design changes and cost overruns as well as university manufacturing limitations, the final proof-of-principle prototype was tested without the application of a water sealant.

The MG performance was characterized by evaluating the active region volumetric torque density, T_v, and active region mass torque density, T_m defined by

$$T_v = T/(\pi r_o^2 d) \qquad (7)$$

$$T_m = T/(m_m + m_s) \qquad (8)$$

where T = peak input torque, r_o = outer MG radius and d = active region stack length, m_m = magnet mass, and m_s = cage rotor lamination mass. The 3-D magnetostatic JMAG computed finite element analysis (FEA) calculated torque density for both the stage-1 and stage-2 MGs are summarized in Table III. Due to the larger airgap radius the stage-1 MG has the highest volumetric torque. But, the stage-1 MG has a larger mechanical support mass. The 3-D FEA calculated torque value shown in Table III is higher than the required minimum value shown in Table I. This is because a design factor, k_s, was used so that any unforeseen discrepancies created during the construction and testing of the proof-of-principle MGs could be accounted for [14, 15]. Table III also shows the computed airgap shear stress in both the inner and outer airgaps. The shear stress values are higher than the values reported for the flux focusing design presented in [21] and significantly higher than for continuously rated PM motors [4].

The mechanical, thermal design as well as testing results for the stage-2 MG are reported in [43]. In the following three sections further design and testing results for the stage-1 MG, not presented in [14] are provided. Then in section VI testing results, as well as a performance comparison discussion, is provided for the dual-stage MG.

III. STAGE-1 MODULATOR DEFLECTION ANALYSIS

To maximize the torque density of a MG, a long axial length is preferred as it then reduces the edge effect [44]. But radial deflection of the cage rotor's ferromagnetic laminations limits the maximum MG axial length. To mitigate deflection the cage rotor modulator is supported using Garolite G10 rectangular bars. As the modulator cage rotor was manufactured as a single lamination piece, the force on each bar was evaluated by computing the force between two consecutive halves of each modulator segment. The area of the force was computed within the 7.8° angular span as shown in Fig. 3. Fig. 4 shows the resulting 2-D magnetostatic FEA calculated force value experienced by each Garolite bar. The sum of the radial force cancels because the design has an even number of modulator slots [45, 46].

The force values shown in Fig. 4 were applied to the Garolite rods and the resulting deflection was computed using an Ansys 3-D FEA model. As the deflection modelling of the individual lamination sheets creates a massive computational burden [14] only one lamination sheet was used to show the impact that the lamination has on air-gap deflection. For example, Fig. 5(a) shows the deflection when there are no laminations present and Fig. 5(b) shows the air-gap deflection when just one lamination is added. Fig. 6 compares the radial and tangential force deflection values for these two cases. Fig. 6 shows that by just adding the one lamination the peak radial deflection reduced by 45% from 0.053 mm to 0.029 mm. Thereby indicating that the deflection mitigation is highly sufficient.

TABLE II. STAGE 1 AND STAGE 2 MAGNETIC GEAR DESIGN VALUES

Description		MG Stage		Unit
		Stage 1	Stage 2	
Inner rotor	Pole-pairs	6	4	-
	Steel pole span	30	-	degree
	Airgap, g_i	0.5	0.5	mm
	Magnet radial length	67	20	mm
Cage rotor	Slots	46	38	-
	Slot span	4.07	4.73	degree
	Radial length	13	8	mm
	Stacking factor	0.95	0.95	-
Outer rotor	Pole-pairs	40	34	-
	Outer radius, r_o	170	65	mm
	Airgap, g_o	1.5	0.5	mm
	Radial length	13	6	mm
	Back iron thickness, l_{bo}	25	15	mm
Axial length, d		50	60	mm

TABLE III. 3-D FEA CALCULATED MAGNETIC GEAR VALUES

Metric		MG Stage		Units
		Stage-1	Stage-2	
Peak input torque, T^{3D}		1,391	227	N·m
Torque density	Volumetric, T_v	306.4	285	N·m/L
	Magnet mass, T_{md}	87.1	65.3	N·m/kg
	Mass, T_m	56.2	53.9	N·m/kg
Airgap shear stress	Inner rotor	32.8	25.1	kN/m^2
	Outer rotor	181	156	kN/m^2
Torque ripple		<1	<1	%
Design factor, k_s		1.31	1.42	-

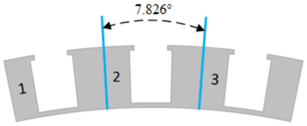

Fig. 3. Ferromagnetic segments with imaginary cuts shown in blue.

This article has been accepted for publication in IEEE Transactions on Energy Conversion. This is the author's version which has not been fully edited and content may change prior to final publication. Citation information: DOI 10.1109/TEC.2022.3190831

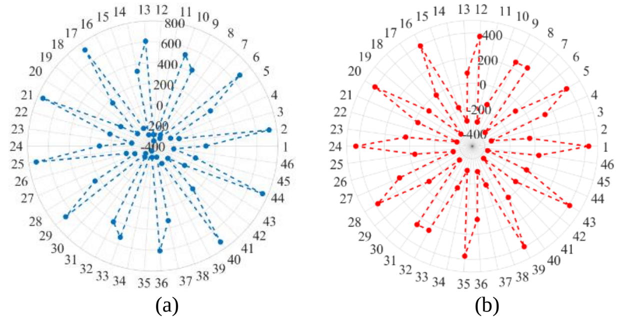

(a) (b)

Fig. 4. (a) 2-D FEA calculated radial force and (b) tangential force applied to each Garolite modulator support bar.

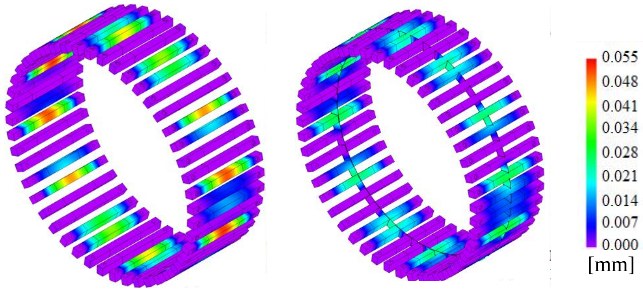

(a) (b)

Fig. 5. 3-D FEA computed radial deflection on the cage rotor Garolite rod support segments when (a) no laminations are present and (b) with one lamination sheet.

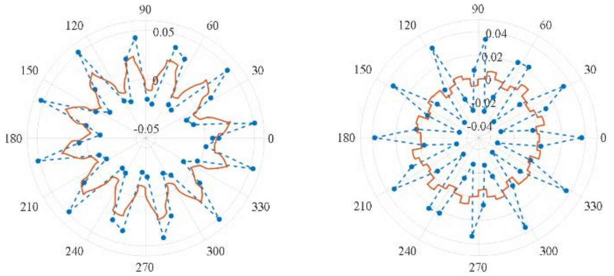

(a) (b)

Fig. 6. (a) Radial and (b) tangential 3-D FEA computed deflection change with angle at axial position z = 25 mm (middle of the active region) for the case when no laminations (blue trace) and one lamination (red trace) is included in the FEA deflection computation.

IV. STAGE 1 MAGNETIC GEAR ASSEMBLY

Fig. 7 shows the assembled stage-1 inner MG rotor and modulation rotor. Fig. 7(b) shows how the inner rotor magnets are sandwiched between the two endplates and Fig. 7(d) shows the G-10 rods after they were inserted into the cage rotor slots (using dry ice). The outer rotor magnets were bonded to the ferromagnetic back-iron using Loctite E-40HT adhesive.

The field and spatial harmonic comparison between the 3-D FEA computed radial airgap field evaluated on the surface of the magnets and the experimental measured inner and outer rotor fields is shown in Fig. 8 and Fig. 9, respectively. An AlphaLab gaussmeter (model GM2) was used for this measurement. The positioning of the gaussmeter probe, at a particular angular location, was determined by using a customized printed paper ruler attached on the outer surface of inner rotor and inner surface of outer rotor. The probe was located at the axial center of the magnet thereby minimizing the axial field component.

Due to the use of the flux-concentration rotor the inner rotor contains more harmonic components than the outer rotor. The inner rotor FEA computed fundamental is in good agreement with measurements. While the measured outer rotor fundamental was 6 % lower than calculated. Using 3-D FEA analysis the discrepancy in the fundamental harmonic component of magnetic flux density can be removed by lowering the magnets residual flux density from B_{rm} = 1.4 T to B_{rm} =1.316 T. The outer rotor magnets were also radially undersized by 0.25 mm, this increased the outer rotor airgap to g_o = 1.75mm. After adjusting the magnet residual flux density and increasing the outer airgap the FEA computed peak static torque reduced to 1,233 N·m, down by 12 %. Table IV shows the stage-1 MG performance metric reduction after accounting for these observed rotor fabrication differences.

If not properly centered large radial forces between the rotors will be created. Also, when inserting the MG rotors, a large axial pull force is created. To provide a controlled assembly mechanism and prevent airgap closure, the rotor assembly jigs shown in Fig. 10 were used. Fig. 10(a) shows the inner rotor retained on the bottom and the modulator rotor being lowered over the inner rotor, whilst Fig. 10(b) shows the outer rotor assembly being axially moved down over the cage modulation rotor. The use of the alignment rods enabled the assembly to be completed without closing the airgap.

The assembled stage-1 MG on the test-stand is shown in Fig. 11. For testing and validation purposes the MG was operated in motoring mode. The high-speed side of the MG was put in speed-control mode and the high-torque low-speed side was put in torque control mode. The PM motor on the left side of Fig. 11 is a 6.6 kW Schneider-Electric PM motor (model BSH-2051) and was connected to the MG's high-speed side via the Dodge Quantis 9.73:1 mechanical gearbox. The low-speed side of the MG was connected to the SEW Eurodrive geared induction motor (model DFV132ML4) with a gear ratio of 33.25:1. The torque on both MG sides were measured using the Himmelstein (model MCRT-48200V) torque transducers.

Fig. 12 shows the FEA and measured inner rotor static torque versus inner rotor mechanical angle. The static test was performed by locking the high-torque MG shaft and using the PM motor to applying torque onto the low torque shaft until the MG pole slipped. The load angle was measured using the PM motor

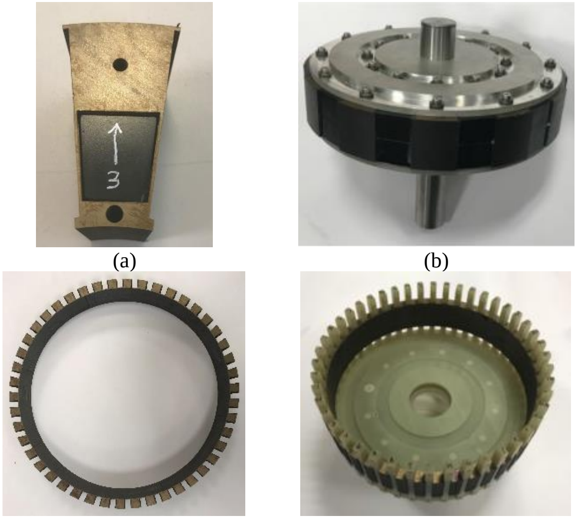

(a) (b) (c) (d)

Fig. 7. (a) One inner rotor magnet and lamination segment, (b) Fully assembled inner rotor, (c) Cage rotor laminations, (d) Fully assembled cage rotor with the Garolite G10 bar supports.

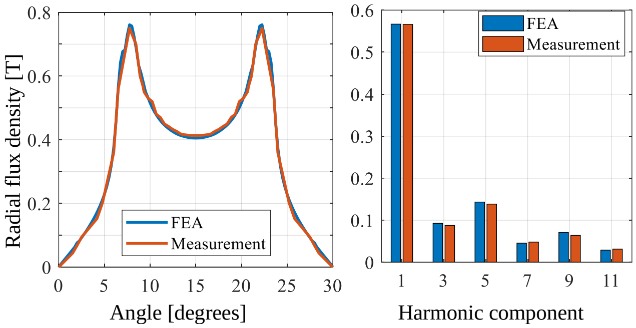

(a) (b)

Fig. 8. (a) Measured and FEA computer radial flux density, B_r, field comparison for one pole of inner rotor, (b) the harmonic components with respect to main harmonic. The field was evaluated at r = 142.9 mm

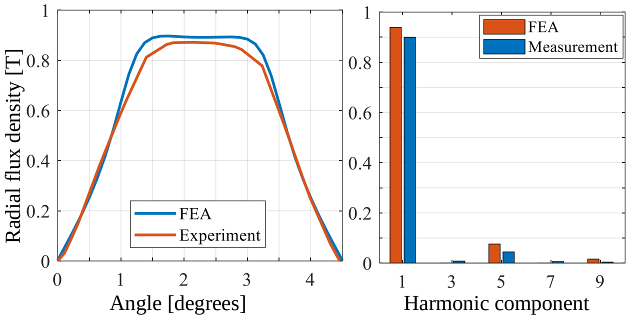

(a) (b)

Fig. 9. (a) Measured and FEA computer radial flux density, B_r, field comparison for one pole of outer rotor, (b) the harmonic components with respect to the main harmonic.

TABLE IV. STAGE-1 EXPERIMENTAL DESIGN RESULTS

Metric		Stage-1		Units
		Adjusted FEA	Measured	
Peak torque	Static, T_{Io}^{3D}	1233	1220	N·m
	Transient at ω_{Io}=45 rpm	-	1106	
Torque density	Volumetric, T_d	271.6	268.7	N·m/L
	Magnet mass, T_m	77.2	76.4	N·m/kg
	Mass, T_m	49.8	49.3	N·m/kg
Airgap shear stress	Inner rotor	58.1	57.5	kN/m^2
	Outer rotor	321	318	kN/m^2
Design factor, k_s		1.16	1.15	-

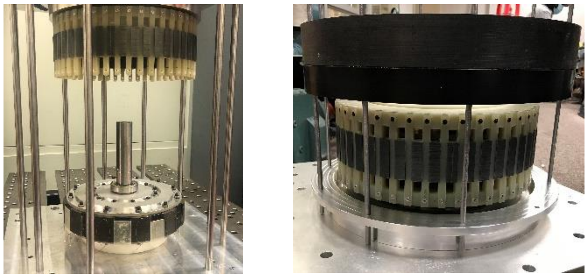

(a) (b)

Fig. 10. (a) Inserting cage modulator over inner rotor and (b) Inserting outer rotor over fixed cage modulator assembly.

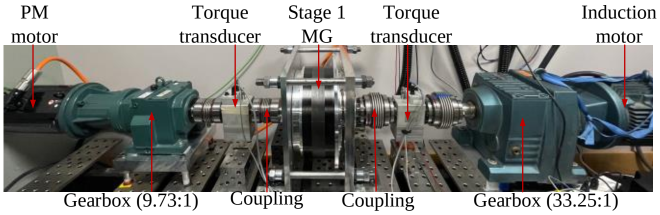

Fig. 11. Stage 1 MG on the test setup.

encoder.

The MG reached a peak measured static torque of T_{Ii} = 183.1 N·m, before pole slipping. Applying the gear ratio multiplier, the high-torque side will be T_{Io} = 1,220.6 N·m which is only 1 % lower than the calculated value stated in Table IV.

Fig. 13 shows the measured input and output torque and power as a function of time when ω_{Io} = 45 r/min and the load torque applied by the induction motor was step changed using the Delta drive (model VFD-150C23A). The PM-motor put regenerative power back to the grid via the Delta active-front-end unit (model AFE-150A23A). Pole slipping was measured to occur when the average input torque exceeded T_{Io} = 1,106 N·m. This is 114 N·m lower than the measured peak static input torque. An average value is stated because the torque ripple makes it difficult to determine the exact pole-slipping value. To manage the overload torque pole-slipping the motor/generator drive will need to incorporate overload detection and remedial strategies to mitigate the overload torque condition [47-51].

Fig. 14(a) shows the calculated time-varying torque at the peak electrical load angle, δ_e = 90˚, and Fig. 14(b) shows the measured time varying torque when δ_e = 56.3˚. The inner rotor

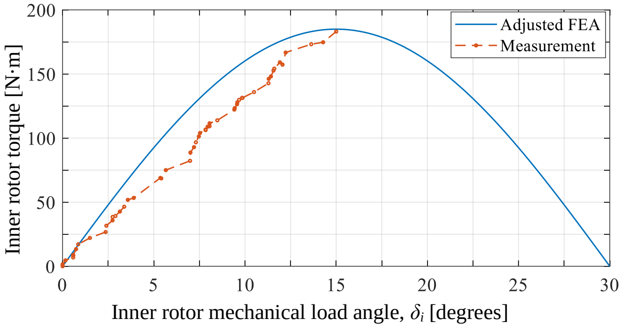

Fig. 12. Static torque comparison between the adjusted 3-D FEA calculated value and measurements.

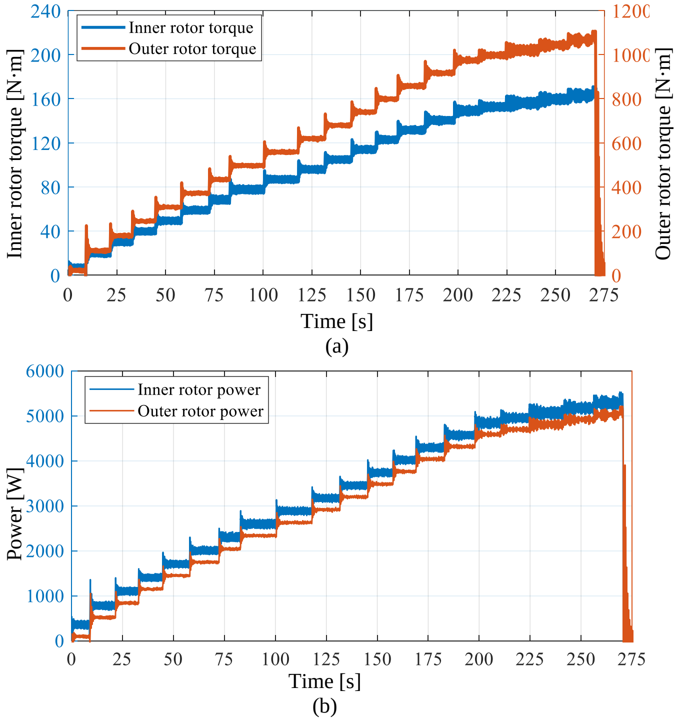

(a)

(b)

Fig. 13. (a) Measured input and output step change torque, (b) power when the rotor speed was maintained at ω_{Io} = 45 r/min.

This article has been accepted for publication in IEEE Transactions on Energy Conversion. This is the author's version which has not been fully edited and content may change prior to final publication. Citation information: DOI 10.1109/TEC.2022.3190831

torque ripple (% of the average torque peak-to-peak value) for the calculated and measured is 0.4 % and 4 %, respectively. Note that the average torque shown in Fig. 14 is 2% lower than that shown in [14] because the MG design was re-calculated with a finer mesh setting.

V. STAGE 1 POWER LOSS AND EFFICIENCY ANALYSIS

The loss within the MG will reduce the peak torque capability. To calculate the impact of loss on the MG torque and efficiency the eddy-current and core loss within the PMs and lamination material were computed using a transient 2-D FEA JMAG model. To calculate the eddy current loss within the PMs, the material conductivity was used. The eddy current and hysteresis losses of the M-19 laminated material were calculated using the specific loss at different frequencies and different magnetic flux values that were provided by the manufacturer. The core loss components are calculated using classical expressions of hysterics and eddy current losses.

In order to determine an appropriate time-step, an electrical frequency analysis for each rotor was conducted.

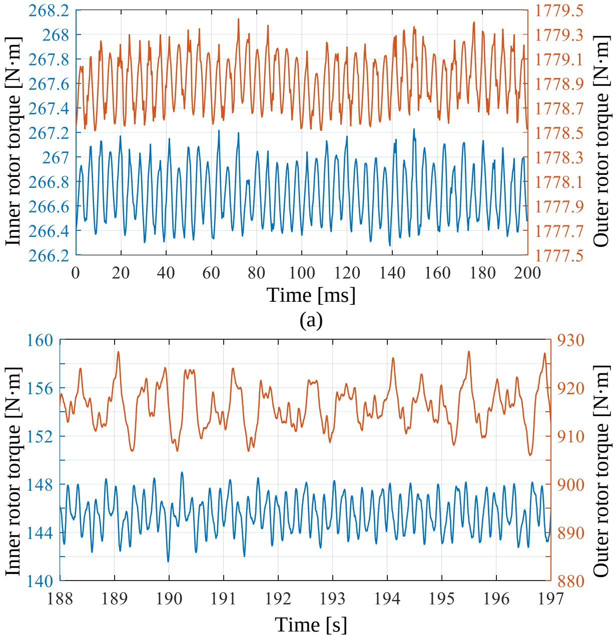

(b)

Fig. 14(a) 2-D FEA calculated inner and outer rotor torque ripple and (b) experimentally measured torque ripple. The starting time at t = 188 s in (b) corresponds to the time shown in Fig. 13.

A. Cage Modulator Electrical Harmonics

The stage-1 MG cage modulator is stationary. Therefore, it sees both inner and outer rotor rotating fields relative to its fixed reference frame. The inner rotor contains p_{Ii} = 6 pole-pairs and is mechanically rotating with an angular speed ω_{Ii}, the mth electrical harmonic created by the inner rotor will be

$$\omega_m = m \cdot p_{Ii} \omega_{Ii} \,. \tag{9}$$

Similarly, as the outer rotor is mechanically rotating with angular speed ω_{Io} it will create an hth electrical harmonic in the outer airgap:

$$\omega_h = h \cdot p_{Io} \omega_{Io} \tag{10}$$

where p_{Io} = 40 pole-pairs. Noting from (3) that $p_{Io}\omega_{Io} = - p_{Ii}\omega_{Ii}$. Then at the peak angular speed, ω_{Io} =45 r/min (f_{Io} =0.75 Hz), the lowest harmonic seen by the stationary cage rotor will be

$$\omega_1^{ce} \;/\; 2\pi = 30\,\text{Hz}. \tag{11}$$

B. Outer Rotor Electrical Harmonics

The rotating field within the outer rotor is created by the inner rotor field. Using a complex Fourier series, the inner rotor's mth spatial harmonic field term, in a stationary reference frame can be described by

$$B_m^{Ii}(r,\theta) = B_m(r) e^{jm \cdot p_{Ii}(\theta - \omega_{Ii} t)} \,,\; m = 1,3,5\ldots \tag{12}$$

The stationary cage rotor slots will create a set of kth spatial frequency permeance terms described by

$$\lambda_k^I(r,\theta) = \lambda_k(r) e^{jk \cdot n_I \theta} \;,\; k = 0, \pm 1, \pm 3, \pm 5\ldots \tag{13}$$

The modulated flux density in the outer rotor can then be described by [52]

$$B_{m,k}^{Io}(r,\theta) = B_m^{Ii}(r,\theta) \lambda_k^I(r,\theta) \,. \tag{14}$$

Substituting (12) and (13) into (14) and rearranging gives

$$B_{m,k}^{Io}(r,\theta) = B_{m,k}(r) e^{j(k \cdot n_I + m \cdot p_{Ii})[\theta - \frac{m p_{Ii}}{(k \cdot n_I + m \cdot p_{Ii})} \cdot \omega_{Ii} t]} \tag{15}$$

where

$$B_{m,k}(r) = B_m(r) \lambda_k(r) \,. \tag{16}$$

Considering (15) the outer rotor spatial harmonic terms are

$$p_{m,k} = k \cdot n_I + m \cdot p_{Ii} \tag{17}$$

and the spatial field will be rotating in the outer airgap with a mechanical angular speed:

$$\omega_{m,k} = \frac{1}{p_{m,k}} [m \cdot p_{Ii}] \omega_{Ii} \,. \tag{18}$$

As the outer rotor is also rotating the mechanical spatial harmonics seen by the outer rotor is the speed difference:

$$\omega_{m,k}^o = \omega_{Io} - \omega_{m,k} \,. \tag{19}$$

The electrical frequency seen by the outer rotor is then

$$\omega_{m,k}^{oe} = p_{m,k} \cdot [\omega_{Io} - \omega_{m,k}] \,. \tag{20}$$

Substituting (18) into (20) and using (3) to write ω_{Ii} in terms of ω_{Io} yields

$$\omega_{m,k}^{oe} = [k \cdot n_I + m \cdot p_{Ii}] \omega_{Io} + [m \cdot p_{Io}] \omega_{Io} \tag{21}$$

using (1) to simplify and rearranging gives

$$\omega_{m,k}^{oe} = n_I \cdot [k + m] \omega_{Io} \,. \tag{22}$$

With n_I = 46 and (m,k) = (1,0) the fundamental electrical frequency seen by the outer rotor when ω_{Io} =45 r/min (f_{Io}=0.75 Hz) is

$$\omega_{1,0}^{oe} \;/\; 2\pi = 34.5\,\text{Hz}. \tag{23}$$

C. Inner Rotor Electrical Harmonics

The inner rotor electrical harmonics can be calculated by considering the modulated field from the outer rotor. Defining the hth spatially harmonic field distributed from the outer rotor as

$$B_h^{Io}(r,\theta) = B_h(r) e^{h \cdot p_{Io}(\theta - \omega_{Io} t)} \,,\; h = 1, 3, 5\ldots \tag{24}$$

This article has been accepted for publication in IEEE Transactions on Energy Conversion. This is the author's version which has not been fully edited and content may change prior to final publication. Citation information: DOI 10.1109/TEC.2022.3190831

where ω_{Io} = inner rotor mechanical angular speed. The modulated magnetic flux density passing into the inner rotor is

$$B^{Ii}_{h,k}(r,\theta) = B^{Io}_{h}(r,\theta)\lambda^{I}_{k}(r,\theta) \tag{25}$$

Substituting (13) and (24) into (25) gives

$$B^{Ii}_{h,k}(r,\theta) = B_{h,k}(r)e^{j(k\cdot n_I + h\cdot p_{Io})[\theta - \frac{h\cdot p_{Io}}{(k\cdot n_I + h\cdot p_{Io})}\cdot\omega^{Io}t]} \tag{26}$$

where

$$B_{h,k}(r) = B_h(r)\lambda_k(r). \tag{27}$$

In this case looking at (26) the modulated spatial harmonic terms in the outer rotor are

$$p_{h,k} = k\cdot n_I + h\cdot p_{Io}. \tag{28}$$

and are rotating with a mechanical angular speed

$$\omega_{h,k} = \frac{1}{p_{h,k}}[h\cdot p_{Io}]\omega_{Io}. \tag{29}$$

Since the inner rotor is rotating at ω_{Ii} the difference in mechanical speed is:

$$\omega^{i}_{h,k} = \omega_{h,k} - \omega_{Ii}. \tag{30}$$

The electrical frequency seen by the inner rotor is then

$$\omega^{ie}_{h,k} = p_{h,k}\cdot[\omega_{h,k} - \omega_{Ii}]. \tag{31}$$

Substituting (29) into (31) and using (3) to write ω_{Ii} in terms of ω_{Io} yields

$$\omega^{ie}_{h,k} = [h\cdot p_{Io}]\cdot\omega_{Io} + [k\cdot n_I + h\cdot p_{Io}]\frac{p_{Io}}{p_{Ii}}\omega_{Io}. \tag{32}$$

using (1) equation (32) simplify to

$$\omega^{ie}_{h,k} = [h+k]\frac{n_I p_{Io}}{p_{Ii}}\cdot\omega_{Io}. \tag{33}$$

With (p_{Ii}, n_I, p_{Io}) = (6, 46, 40) and (m,k) = (1,0), the fundamental frequency when f_{Io} =0.75 Hz (ω_{Io} =45 r/min) is

$$f^{ie}_{1,1} = 230\,\text{Hz}. \tag{34}$$

D. Calculated Stage-1 MG Loss and Efficiency

Within the MG, the cage rotor experiences the lowest rotor frequency, which is given by (11). This gives the electrical period that needs to be simulated to capture a full hysteresis loop. It was determined that by using a sampling frequency 20 times that given by (34), such that $f_s = 20\cdot\omega^{ie}_{1,1}/2\pi \approx 4\text{kHz}$ the FEA computed loss changed by less than 1%. Therefore, using this a time-step size of t_s = 250μs (f_s = 4kHz) with ω_{Ii} = 45 r/min the 2-D FEA loss values shown in Table V were obtained. The calculations show that the loss within the inner rotor is contained within the tangential magnets. This is because the radial magnets are embedded further into the laminations. This effect can be more clearly seen in Fig. 15 which shows the 2-D transient FEA calculated cross-sectional cut-through view of the eddy current loss contour plot at a steady-state time step value. The loss within the inner rotor magnets is created by the relative rotation of the p_3 outer rotor pole-pairs, because the outer rotor magnet field path is small the loss is concentrated near the surface of the magnets. In contrast the loss in the outer rotor magnets is throughout the magnets. This is a consequence of the inner rotor magnets having a much larger field path thereby allowing the inner rotor magnet field to fully penetrate the outer magnets.

TABLE V. THE 2-D FEA COMPUTED MAGNETIC GEAR COMPONENT LOSS

Component		Loss [W]	Loss density [W/m^3]
Inner rotor	Tangential magnets	12.9	11652
	Radial magnets	0.0	0.0
	Lamination eddy current	0.8	1886
	Lamination hysteresis	0.7	
Cage rotor	Eddy current	2.3	47857
	Hysteresis	12.2	
Outer rotor	All magnets	17.4	24186
	Back iron eddy current	0.9	4464
	Back iron hysteresis	5.5	
Total	Eddy current loss, P_{e1}	34.3	16054
	Hysteresis loss, P_{h1}	18.4	6901

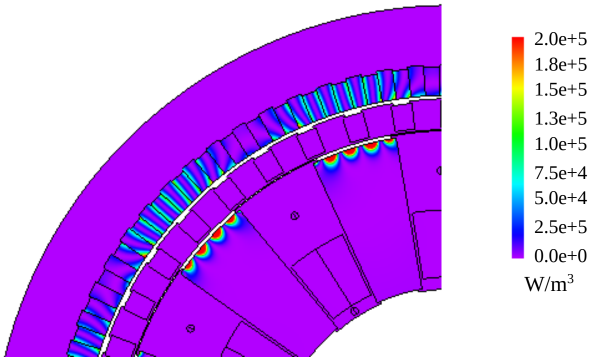

Fig. 15. Joule loss density distribution within the PMs when ω_{Io} = 45 r/min.

In motoring mode, T_{Ii}, is the input torque, (low-torque side) and T_{Io} is the output torque (high-torque side). In this case the electrical efficiency is defined as:

$$\eta_I = \frac{T_{Io}(\omega_{Ii})\cdot\omega_{Io}}{T_{Io}(\omega_{Ii})\omega_{Io} + P_{sI}(\omega_{Ii})} \tag{35}$$

where P_{sI} are the total calculated losses within the MG. Using the loss values shown in Table V the stage-1 MG electrical efficiency is computed to be η_I = 99%.

E. Measured Stage 1 MG Loss and Efficiency

The experimental test setup shown in Fig. 11, was used to compute the losses and efficiency. The power was applied on the high-speed side and so in motoring mode the stage-1 MG power relation is

$$T_{Ii}\cdot\omega_{Ii} = T_{Io}(\omega_{Ii})\cdot\omega_{Io} + P_{sI}(\omega_{Ii}). \tag{36}$$

The bracketed torque and power loss terms in (36) denote that they are functions of the input speed. The power loss is expressed as a function of angular speed, ω_{Io}. The loss within the MG can be separated into components such that

$$P_{sI}(\omega_{Io}) = P_{Ih}(\omega_{Io}) + P_{Ie}(\omega_{Io}) + P_{Im}(\omega_{Io}) \tag{37}$$

where P_{Ih} = hysteresis losses and P_{Ie} = eddy current losses and P_{Im} = mechanical losses (bearings and windage). Fig. 16 shows the measured no-load loss within the MG as a function of angular speed, ω_{Io}. The loss curve fit is described by:

$$P_{s1}(\omega_{Io}) = 2.73\omega_{Io} + 0.065\omega^2_{Io} \tag{38}$$

where ω_{Io} has units of r/min. At ω_{Io} = 45 r/min the measured loss was P_{s1} = 255 W. This is 4.8 × higher than FEA calculated value at the same speed. The measured loss also includes the mechanical frictional loss. Therefore, the increase in loss is partially attributed to the expected rotary friction and windage loss as well as frictional loss created by manufacturing tolerance errors that resulted in additional radial force pressing on the outer rings of the bearing. However, despite using non-conductive end plate supports, the majority of excessive loss is believed to be due to the edge-effects of the fields that still leaking out and entering into the metallic (Aluminum) MG support end-plate structure. To mitigate the loss within support structure, they can be made from Garolite. The only foreseen limitations for Garolite would be the availability of large billets of material for thicker components and the moisture absorption in marine applications.

As expected, Fig. 17 shows that the measured loss does not significantly change with load. The decoupling of the MG loss with load was previously noted in [53, 54]. The decoupling of loss with load allows the MG efficiency to be characterized using only no-load data.

Substituting (36) into (35) and using (3) the MG efficiency can be evaluating experimentally by using the ratio of torque:

$$\eta_I(\omega_{Ii}) = \frac{T_{Io}(\omega_{Ii}) \cdot \omega_{Io}}{T_{Ii} \cdot \omega_{Ii}} \tag{39}$$

The loss reduces the high-speed side torque, T_{Ii}. Equation (39) is valid because the speed-ratio must be synchronous when not pole-slipping. Noting that the loss does not change with load allows the no-load loss to be used to map the efficiency as a function of angular speed and load. In generating mode power and efficiency are described by

$$T_{Ii}(\omega_{Io}) \cdot \omega_{Ii} = T_{Io}\omega_{Io} - P_{sI}(\omega_{Io}) \tag{40}$$

$$\eta_I(\omega_{Io}) = \frac{T_{Ii}(\omega_{Io}) \cdot \omega_{Ii}}{T_{Io}\omega_{Io}} \tag{41}$$

Substituting (40) into (41) gives

$$\eta_I(\omega_{Io}) = 1 - \frac{P_{sI}(\omega_{Io})}{T_{Io}\omega_{Io}} \tag{42}$$

Equation (42) enabled the efficiency map contour plot shown in Fig. 18 to be created from the curve fit loss data. At the peak torque, T_{Io} = 1,220 N·m and ω_{Io} = 45 r/min, the efficiency is η = 95.5 %. Note that the efficiency calculation used to create Fig. 18 does not account for the reduction in slip torque on the input shaft caused by elevated temperatures. This would only affect the efficiency near the peak torque.

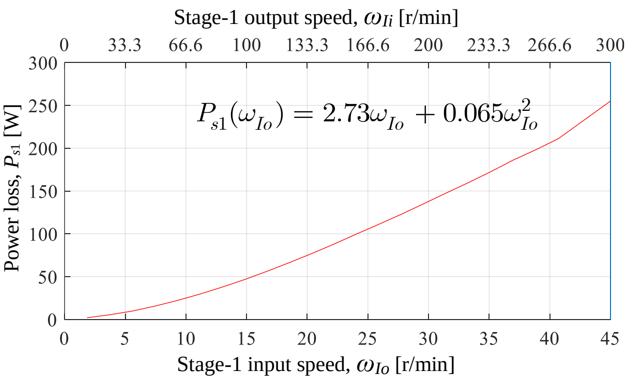

Fig. 16. Measured power loss of the stage-1 MG when at no-load.

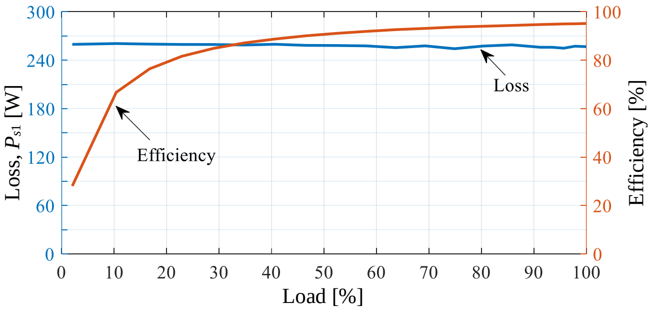

Fig. 17. Measured stage-1 MG measured efficiency and power loss as a function of peak load percentage when the input speed is ω_3 = 45 r/min.

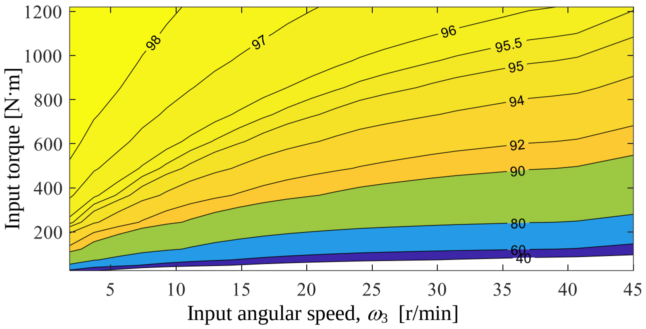

Fig. 18. Contour plot of efficiency with angular speed and applied torque

VI. DUAL-STAGE MAGNETIC GEAR EXPERIMENTAL TESTING

The dual-stage MG on the test-stand is shown in Fig. 19. As the motor integrated stage-2 MG generator had a failure during testing the generator was not directly connected to the stage-2 MG output shaft (like shown in Fig. 2). But instead, the high-speed stage-2 MG, shown on the left in Fig. 19, was connected to the Himmelstein torque transducer and then a Fanuc PM generator (model αis200/2500). The Fanuc PM motor without mechanical gearbox was used because it could directly provide the required high-speed input and torque. The stage-2 MG was water-cooled using a cooling jacket. The right side of the MG test-stand remained unchanged from the stage-1 MG test setup that was described in the prior section. The setup was tested by operating the MG in motoring mode. The induction motor was put in torque control mode and the PM motor was set to speed control mode. The measured no-load loss as a function of the input angular speed, ω_{Io}, is shown in Fig. 20. The loss due to the stage-1 and stage-2 MG is also shown. Note that the stage-2 MG loss was indirectly computed by subtracting the stage-1 MG loss from the dual-stage MG loss.

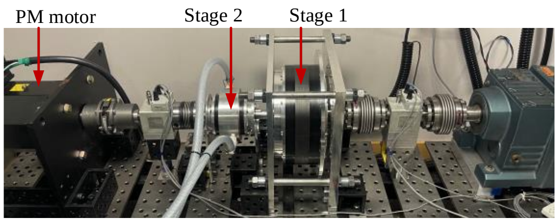

Fig. 19. The dual-stage MG on the test-stand. For testing validation purposes the MG was operating in motoring mode.

This article has been accepted for publication in IEEE Transactions on Energy Conversion. This is the author's version which has not been fully edited and content may change prior to final publication. Citation information: DOI 10.1109/TEC.2022.3190831

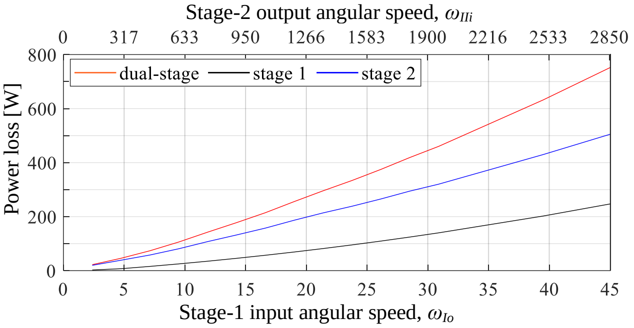

Fig. 20. Measured power loss for the dual-stage MG, $P_s(\omega_{Io})$, also shown in the stage-1 MG measured loss, $P_{sI}(\omega_{Io})$. The stage-2 MG power loss, $P_{sII}(\omega_{Io})$ is the difference between the dual and stage-1 loss plot. Note that the stage-2 output speed is shown on the top x-axis.

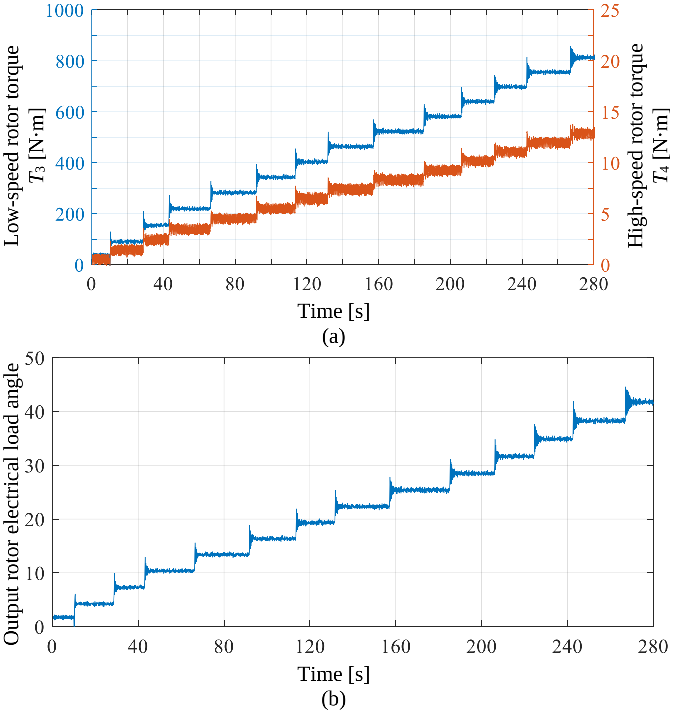

Fig. 21. (a) Measured step change torque on the input and output dual stage MG shafts when operating at a constant input angular speed of ω_{Io} = 15.8 r/min (which corresponds to ω_{IIi} = 1000 r/min), (b) Output rotor electrical load angle corresponding to the step change torque in (a).

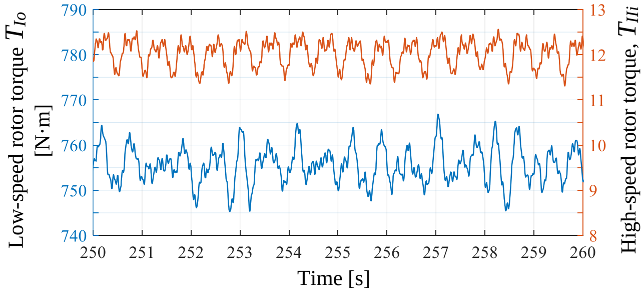

Fig. 22. Measured dual-stage MG high-speed rotor torque, T_{Ii} and low-speed rotor torque, T_{Io}, when the load angle is δ = 38.3°.

Fig. 21 shows the measured input and output torque change for the dual-stage MG. As both the stage-1 and stage-2 MGs were previously individually pole slipped, the dual-stage MG torque was only step increased to T_{Ii} = 815 N·m. The measured torque ripple at an electrical load angle $\delta_e = 38.3^\circ$ is shown in Fig. 22. The torque ripple on the high-torque and low-torque shaft was measured to be T_{rh} = 22 N·m (2.6%) and T_{rl} = 1.3 N·m (10%), respectively. The higher torque ripple on the low-torque side is a consequence of the addition of the torque ripple from both MG stages as well as the amplified torque ripple coming from the load induction motor.

The power flow relationship for the dual-stage MG experimental setup when in generator mode is

$$T_{IIi}(\omega_{Io})\cdot\omega_{IIi} = T_{Io}\omega_{Io} - P_s(\omega_{Io}) \tag{43}$$

where P_s is the electrical and mechanical loss associated with both MG stages and T_{IIi} = stage-2 MG low-torque output, ω_{IIi} = stage 2 MG high-speed output. The change in torque and loss are written as function of input angular speed, ω_{Io}. As before the no-load power loss measurement provides a means of characterizing the efficiency over the torque-speed range. The dual-stage MG efficiency is

$$\eta(\omega_{Io}) = \frac{T_{IIi}(\omega_{Io})\cdot\omega_{IIi}}{T_{Io}\cdot\omega_{Io}} \tag{44}$$

The loss reduces the high-speed side torque, T_{IIi}. Substituting (43) into (44) gives

$$\eta(\omega_{Io}) = 1 - \frac{P_s(\omega_{Io})}{T_{Io}\omega_{Io}} \tag{45}$$

Using (45) with the measured, and curve fitted loss data, the efficiency map, as shown in Fig. 23, was created. The efficiency when ω_{Io} = 45 r/min and at the peak load condition is η = 87 %.

A summary of the performance metrics for the dual-stage MG is shown in Table VI. As the stage-2 MG makes up only 15% of the total volume for the dual-stage MG reduces down to 231 Nm/L from 268.7 for just the stage-1 MG. The overall volumetric torque density for the dual-stage stays high. Table VII shows the performance characteristics for a representative sized Sumitomo gearbox. The mass was stated as approximate in the data sheet and the length and diameter had to be estimated from the provided geometric information. It can be noted that the MGs volumetric torque density is around 13 to 36 lower than the mechanical gear equivalent. The mass torque density for the MG is likely to be approximately equivalent to the mechanical gear. This is because the MG relies on a lot of light weight non-magnetic components. Further work on improving efficiency is still needed.

TABLE VI. DUAL-STAGE MG PERFORMANCE METRICS

Metric		Measured	Calculated	Unit	% Difference
Input torque, T_{Io}		1220	1233	N·m	-1
Torque density	Volumetric, T_d	228.6	231.1	N·m/L	-1
	Magnet mass, T_m	62.8	63.4	N·m/kg	-1
	Mass, T_m	42.1	42.6	N·m/kg	-1
Efficiency at ω_{Io} = 45 r/min		87	98	%	-11

TABLE VII. SUMITOMO GEARBOX CHARACTERISTICS [55]

Gear ratio		**59**	**59**	**59**	**43**	**43**	**Units**
Output torque		1118	1355	1751	878	1197	Nm
Input power		**3.704**	**4.48**	**5.83**	**4.00**	**5.53**	kW
Input speed		1750	1750	1750	1750	1750	r/min
Output RPM		29.7	29.7	29.7	40.7	40.7	r/min
Efficiency		94	94	93	94	92	%
Approx. mass		44	84	84	44	44	kg
Approx. axial length		145	150	150	145	145	Mm
Approx. diameter		170	217	217	170	170	mm
Torque density	Volumetric	340	344	315	267	364	Nm/L
	Mass	25.4	16.1	20.8	20.0	27.2	Nm/kg

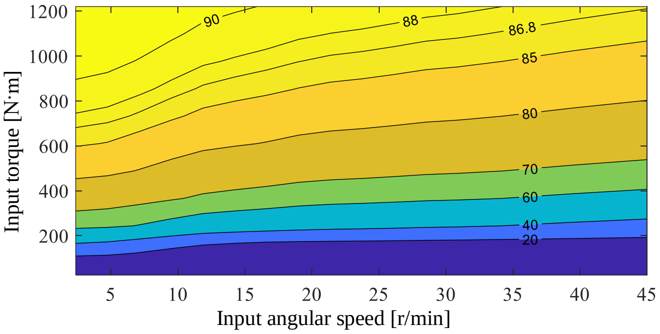

Fig. 23. Contour plot showing the measured dual-stage MG efficiency

VII. CONCLUSION

This paper has presented the experimental testing results for a 63.3:1 dual-stage MG as well as testing and further design details for the stage-1 MG. The stage-1 MG had a calculated and measured peak torque of 1233 N·m and 1220 N·m, respectively. This corresponds to a calculated and measured active region torque density of 272 N·m/L, and 269 N·m/L, respectively. The dual-stage MG had an active region volumetric and mass torque density of 228.6 N·m/L and 42.6 Nm/kg respectively. The peak efficiency for the stage-1 MG was measured to be 95.5% and the peak efficiency for the dual-stage MG dropped to 86.8%. There were significantly higher measured losses than expected. It is believed that the majority of these losses were contained within the conductive support parts of the magnetic gear. This paper indicates that a dual-stage MG has the ability to be designed to be competitive in performance with a comparable mechanical gear. Further experimental prototype work is needed to demonstrate improved loss mitigation.

VIII. ACKNOWLEDGMENT

The authors would gratefully like to thank the Ansys and JMAG Corporation for the use of their FEA software.

IX. REFERENCES

[1] S. Benelghali, M. E. H. Benbouzid, and J. F. Charpentier, "Generator Systems for Marine Current Turbine Applications: A Comparative Study," *IEEE Journal of Oceanic Engineering,* vol. 37, no. 3, pp. 554-563, 2012.

[2] K. Touimi, M. Benbouzid, and P. Tavner, "Tidal stream turbines: With or without a Gearbox?," *Ocean Engineering,* vol. 170, pp. 74-88, 2018/12/15/ 2018.

[3] W. Musial, S. Butterfield, and B. McNiff, "Improving Wind Turbine Gearbox Reliability," National Renewable Energy Laboratory, NREL/CP-500-41548, , May 2007.

[4] M. A. Mueller, H. Polinder, and N. Baker, "Current and novel electrical generator technology for wave energy converters," in *IEEE Elect. Mach. Dri. Conf.*, Antalya, Turkey 2007, pp. 1401 - 1406

[5] T. J. E. Miller, *Brushless Permanent-Magnet and Reluctance Motor Drives*. Oxford University Press, 1989.

[6] J. Z. Bird, "A Review of Electric Aircraft Drivetrain Motor Technology," *IEEE Transactions on Magnetics,* pp. 1-1, 2021.

[7] F. Wu and A. M. El-Refaie, "Permanent magnet vernier machine: a review," *IET Electric Power Applications,* vol. 13, no. 2, pp. 127-137, 2019.

[8] D. Li, R. Qu, and T. A. Lipo, "High-Power-Factor Vernier Permanent-Magnet Machines," *IEEE Transactions on Industry Applications,* vol. 50, no. 6, pp. 3664-3674, 2014.

[9] D. McMillan and G. W. Ault, "Techno-Economic Comparison of Operational Aspects for Direct Drive and Gearbox-Driven Wind Turbines," *IEEE Transactions on Energy Conversion,* vol. 25, no. 1, pp. 191-198, 2010.

[10] D. S. Jenne and Y.-H. Yu, "Levelized Cost of Energy Analysis of Marine and Hydrokinetic Reference Models
National Renewable Energy Laboratory," presented at the 3rd Marine Energy Technology Symposium (METS 2015), Washington, D.C., April 27–29, 2015.

[11] L. Shah, A. Cruden, and B. W. Williams, "A variable speed magnetic gear box using contra-rotating input shafts," *IEEE Trans. Mag.,* vol. 47, no. 2, pp. 431-438, 2011.

[12] J. Bird, "Marine hydrokinetic power take-off using magnetic gearing," presented at the 2nd Marine Energy Technology Symposium, Seattle, WA, April 15-18, 2014.

[13] B. McGilton, M. Mueller, and A. McDonald, "Review of magnetic gear technologies and their applications in marine energy," in *5th IET Intern. Conf. Renew. Power Gen.*, London, UK, 21-23 Sept. 2016 2016, pp. 1-6.

[14] H. Baninajar, J. Z. Bird, S. Modaresahmadi, and W. Williams, "Electromagnetic and mechanical design of a hermetically sealed magnetic gear for a marine hydrokinetic generator," presented at the IEEE Energy Conv. Cong. Expo., Portland, OR, 2018.

[15] H. Baninajar, J. Z. Bird, S. Modaresahmadi, and W. Williams, "Electromagnetic Design and Assembly Analysis of a Halbach Rotor Magnetic Gear for a Marine Hydrokinetic Application," in *2019 IEEE Energy Conversion Congress and Exposition (ECCE)*, 29 Sept.-3 Oct. 2019 2019, pp. 732-739.

[16] M. Johnson, M. C. Gardner, H. A. Toliyat, S. Englebretson, W. Ouyang, and C. Tschida, "Design, Construction, and Analysis of a Large-Scale Inner Stator Radial Flux Magnetically Geared Generator for Wave Energy Conversion," *IEEE Transactions on Industry Applications,* vol. 54, no. 4, pp. 3305-3314, 2018.

[17] M. Bahrami Kouhshahi, V. M. Acharya, M. Calvin, J. Z. Bird, and W. Williams, "Designing and experimentally testing a flux-focusing axial flux magnetic gear for an ocean generator application," *IET Electric Power Applications,* vol. 13, no. 8, pp. 1212-1218, 2019.

[18] M. B. Kouhshahi *et al.*, "An Axial Flux Focusing Magnetically Geared Generator for Low Input Speed Applications," *IEEE Transactions on Industry Applications,* vol. 56, no. 1, pp. 138-147, 2020.

[19] K. Atallah, S. D. Calverley, and D. Howe, "Design, analysis and realisation of a high-performance magnetic gear," *IEE Proc.-Electr. Power Appl.,* vol. 151, no. 2, pp. 135-143, 2004.

[20] T. B. Martin, "Magnetic Transmission," USA Patent 3,378,710, 1968.

[21] K. K. Uppalapati, J. Z. Bird, J. Wright, J. Pitchard, M. Calvin, and W. Williams, "A magnetic gearbox with an active region torque density of 239Nm/L," *IEEE Trans. Ind. Appl.,* vol. 54, no. 2, pp. 1331-1338, April 2018.

[22] K. Li and J. Z. Bird, "A review of the volumetric torque density of rotary magnetic gear designs," in *XIII International Conference on Electrical Machines (ICEM), ,* Alexandroupoli, Greece, 2018, pp. 2016-2022.

[23] B. Praslicka, M. C. Gardner, M. Johnson, and H. A. Toliyat, "Review and Analysis of Coaxial Magnetic Gear Pole Pair Count Selection Effects," *IEEE Journal of Emerging and Selected Topics in Power Electronics,* pp. 1-1, 2021.

[24] A. B. Kjaer, S. Korsgaard, S. S. Nielsen, L. Demsa, and P. O. Rasmussen, "Design, Fabrication, Test, and Benchmark of a Magnetically Geared Permanent Magnet Generator for Wind Power Generation," *IEEE Transactions on Energy Conversion,* vol. 35, no. 1, pp. 24-32, 2020.

[25] K. Nao, M. Shiono, and K. Suzuki, "Study on the Gear Ratio for a Tidal Current Power Generation System Using the MPPT Control Method," presented at the Twenty-first International Offshore and Polar Engineering Conference, Maui, Hawaii, USA, June 2011.

[26] S. Saeidtehrani, P. Lomonaco, A. Hagmüller, and M. L.evites-Ginsburg, "Application of a simulation model for a heave type wave energy converter," presented at the 12th Eoro. Wave Tidal Energy Conf., Cork, Ireland, 2017.

[27] R. G. Coe, G. Bacelli, and D. Forbush, "A practical approach to wave energy modeling and control," *Renewable and Sustainable Energy Reviews,* vol. 142, p. 110791, 2021/05/01/ 2021.

[28] J. Zhang and Q. Zhang, "Design and analysis of a two-stage transmission magnetic-geared machine," *IEEJ Trans. Elec. Elec. Eng.,* vol. 15, pp. 151–156, 2020.

[29] M. Filippini and P. Alotto, "Coaxial Magnetic Gear Design and Optimization," *IEEE Transactions on Industrial Electronics,* vol. 64, no. 12, pp. 9934-9942, 2017.

[30] A. Floris, A. Serpi, M. Porru, G. Fois, and A. Damiano, "Design of a Double-Stage Magnetic Gear for High-Speed Electric Propulsion

Systems," in *2018 XIII International Conference on Electrical Machines (ICEM)*, 3-6 Sept. 2018 2018, pp. 670-676.

[31] A. Floris, A. Serpi, A. Damiano, and I. Hahn, "Torque Harmonics Minimization of Double-Stage Magnetic Gear Transmission System," in *IECON 2019 - 45th Annual Conference of the IEEE Industrial Electronics Society*, 14-17 Oct. 2019 2019, vol. 1, pp. 2751-2757.

[32] K. Li, "An Investigation into the Torque Capabilities of High Gear Ratio Magnetic Gearboxes," Ph.D. Dissertation, Electrical and Computer Engineering, Univ. N.C. Charlotte, 2018.

[33] J. Bird and W. William, "Advanced High Torque Density Magnetically Geared Generator," Department of Energy, Energy Efficiency & Renewable Energy, Grant # DE-EE0006801, 2018.

[34] M. Desvaux, B. Multon, H. B. Ahmed, S. Sire, A. Fasquelle, and D. Laloy, "Gear ratio optimization of a full magnetic indirect drive chain for wind turbine applications," in *2017 Twelfth International Conference on Ecological Vehicles and Renewable Energies (EVER)*, 11-13 April 2017 2017, pp. 1-9.

[35] K. Li, S. Modaresahmadi, W. B. Williams, J. Z. Bird, J. D. Wright, and D. Barnett, "Electromagnetic Analysis and Experimental Testing of a Flux Focusing Wind Turbine Magnetic Gearbox," *IEEE Transactions on Energy Conversion,* vol. 34, no. 3, pp. 1512-1521, 2019.

[36] M. C. Gardner, M. Johnson, and H. A. Toliyat, "Analysis of High Gear Ratio Capabilities for Single-Stage, Series Multistage, and Compound Differential Coaxial Magnetic Gears," *IEEE Transactions on Energy Conversion,* vol. 34, no. 2, pp. 665-672, 2019.

[37] E. Park, C. Kim, S. Jung, and Y. Kim, "Dual Magnetic Gear for Improved Power Density in High-Gear-Ratio Applications," in *2018 21st International Conference on Electrical Machines and Systems (ICEMS)*, 7-10 Oct. 2018 2018, pp. 2529-2532.

[38] C.-H. Kim, S.-Y. Jung, and Y.-J. Kim, "A comparative analysis of power density for single-stage and dual-stage magnetic gear with rare-earth magnets and non rare-earth magnets," *International Journal of Applied Electromagnetics and Mechanics,* vol. 51, pp. 83-89, 2016.

[39] K. Li, S. Modaresahmadi, W. B. Williams, J. Z. Bird, J. D. Wright, and D. Barnett, "Electromagnetic analysis and experimental testing of a flux focusing wind turbine magnetic gearbox," *IEEE Trans. Energy Conv.*, vol. 34, no. 3, pp. 1512-1521, Sept. 2019.

[40] B. D. Hibbs and B. X. Phan, "Flux Concentrator for ironless motors," USA Patent US 2010/0181858 A1, Jul. 22 2010.

[41] K. Li *et al.*, "Analysis and Testing of a Coaxial Magnetic Gearbox with Flux Concentration Halbach Rotors," *IEEE Trans. Magn.,* 2017.

[42] H. Y. Wong, J. Z. Bird, S. Modaresahmadi, and W. Williams, "Comparative Analysis of a Coaxial Magnetic Gear With a Flux Concentration Rotor and Consequent Pole Rotor Typology," *IEEE Transactions on Magnetics*, vol. 54, no. 11, pp. 1-5, 2018.

[43] H. Baninajar, S. Modaresahmadi, H. Y. Wong, J. Z. Bird, W. Williams, and B. Dechant, "Designing a Halbach Rotor Magnetic Gear for a Marine Hydrokinetic Generator," *Submitted to IEEE Trans. Ind. Appl.* , 2021.

[44] S. Gerber and R. Wang, "Analysis of the end-effects in magnetic gears and magnetically geared machines," in *2014 International Conference on Electrical Machines (ICEM)*, 2-5 Sept. 2014 2014, pp. 396-402.

[45] C. J. Agenbac, D. N. J. E. , R.-. Wang, and S. Gerber, "Force and vibration analysis of magnetic gears," presented at the XIII Intern. Conf. Elect. Mach., Alexandroupoli,Greece 2018.

[46] D. C. Hanselman, "Effect of skew, pole count and slot count on brushless motor radial force, cogging torque and back EMF," *IEE Proceedings - Electric Power Applications*, vol. 144, no. 5, pp. 325-330.

[47] R. G. Montague, C. M. Bingham, and K. Atallah, "Magnetic gear overload detection and remedial strategies for servo-drive systems," in *SPEEDAM 2010*, 14-16 June 2010 2010, pp. 523-528.

[48] R. G. Montague, C. M. Bingham, and K. Atallah, "Magnetic gear dynamics for servo control," in *Melecon 2010 - 2010 15th IEEE Mediterranean Electrotechnical Conference*, 26-28 April 2010 2010, pp. 1192-1197.

[49] M. Desvaux, R. L. G. Latimier, B. Multon, S. Sire, and H. B. Ahmed, "Analysis of the dynamic behaviour of magnetic gear with nonlinear modelling for large wind turbines," in *2016 XXII International Conference on Electrical Machines (ICEM)*, 4-7 Sept. 2016 2016, pp. 1332-1338.

[50] R. Montague and -. C. Bingham, "- Nonlinear Control of Magnetically-geared Drive-trains," - *International Journal of Automation and* Computing, Vol. 10, no. 4, pp. 319, 2013.

[51] N. W. Frank, S. Pakdelian, and H. A. Toliyat, "Passive Suppression of Transient Oscillations in the Concentric Planetary Magnetic Gear," *IEEE Transactions on Energy Conversion,* vol. 26, no. 3, pp. 933-939, 2011.

[52] K. Atallah and D. Howe, "A novel high-performance magnetic gear," *IEEE Transactions on Magnetics,* vol. 37, no. 4, pp. 2844-2846, 2001.

[53] M. Fukuoka, K. Nakamura, and O. Ichinokura, "Experimental Tests and Efficiency Improvement of Surface Permanent Magnet Magnetic Gear," *IEEJ Journal of Industry Applications,* vol. 3, no. 1, pp. 62-67, 2014.

[54] M. C. Gardner, M. Johnson, and H. A. Toliyat, "Performance Impacts of Practical Fabrication Tradeoffs for a Radial Flux Coaxial Magnetic Gear with Halbach Arrays and Air Cores," presented at the IEEE Energy Conversion Congress and Exposition (ECCE), Baltimore, MD, USA, , 2019.

[55] *Cyclo 6000 Speed Reducer Catalog*, Sumitomo Machinary Corporation of America, Catalog # 03.601.50.010, 2015.